Annu. Rev. Phys. Chem. 1994. 45: 401–38

KINETICS OF SURFACE GROWTH: Phenomenology, Scaling, and Mechanisms of Smoothening and Roughening

William M. Tong and R. Stanley Williams

Department of Chemistry and Biochemistry, University of California Los Angeles, Los Angeles, California 90024-1569

KEY WORDS: deposition, etching, morphology, topography

INTRODUCTION

The growth of solid surfaces via vapor phase processes can be viewed as proceeding in either of two directions: outward by physical or chemical deposition or inward by physical or chemical etching. Figure 1 is a schematic illustration of the evolution of a surface, $S(\mathbf{r}, t)$, where S is the z-coordinate of the growing surface at the position $\mathbf{r} = (x, y)$ and time t, and the initial condition $S(\mathbf{r}) = 0$ at $t = 0$ corresponds to initiating the growth on a perfectly flat surface. The average value of the new surface height at any particular time $\langle S(\mathbf{r}) \rangle$ corresponds to the amount of material added to or removed from the original surface. As illustrated in Figure 1, surfaces typically roughen during growth. Many technological applications in optics and electronics require extremely smooth surfaces, and at present, both areas are hampered by inherent roughness resulting from growth processes. A qualitative understanding of how growth mechanisms affect surface morphology is very useful, but to be able to optimize grown structures, a method to predict surface topology quantitatively will be required. Because rough surfaces are inherently very complex and do not appear to have underlying symmetry constraints to simplify mathematical

0066-426X/94/1101-0401$05.00

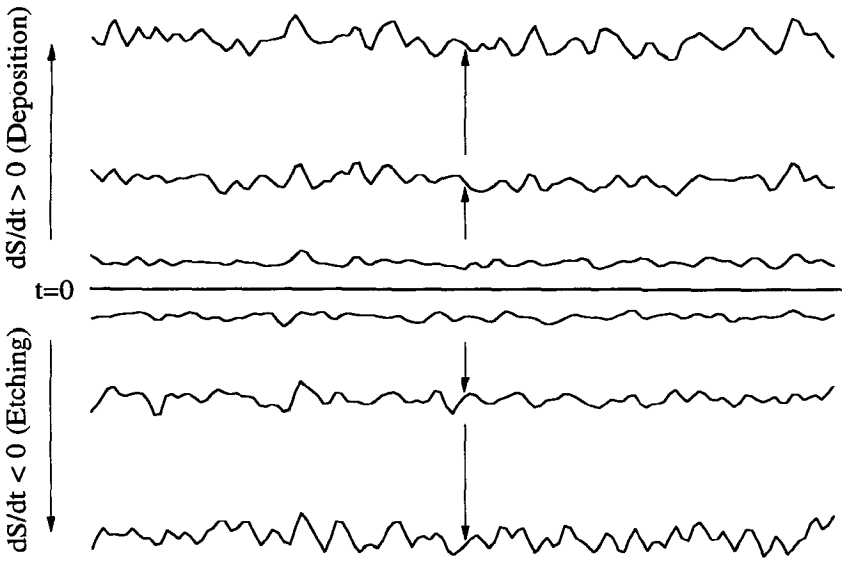

Figure 1 A side view of a solid surface S at various times as it grows outward because of deposition or inward because of etching. The surface evolves roughness as it grows.

modeling, a predictive treatment may appear hopeless. However, recent theoretical and experimental developments have shown that the fundamental molecular-scale phenomena that are involved in surface growth are common to all deposition and etching processes that involve vapor-solid interactions and that these processes leave a definite signature in the topology of the surface. Thus, a unified framework for calculating details of surface topography may soon be constructed that incorporates such varied growth methods as sputter deposition, evaporative techniques, including molecular beam epitaxy (MBE) of crystalline materials, chemical vapor deposition (CVD), ion sputter-etching, dry chemical etching, and plasma etching as special cases. After a brief historical perspective on studies of the development of surface morphology, this review presents a snapshot of current developments in the quantitative classification and understanding of the surface topography that results from growth processes that add or remove many monolayers of a solid material. The structure of the solid below the surface will not be addressed.

The classification scheme most often invoked to understand epitaxial film deposition was proposed over three decades ago by Bauer (1). This paradigm recognized three processes, two of which are topologically distinct, that have been named after their original investigators: Frank–van der Merwe (FM) for monolayer-by-monolayer growth (2), Volmer-

Weber (VW) for three-dimensional (3D) crystallite formation (3), and Stranski-Krastanov (SK) for growth of an initial uniform layer followed by 3D crystallite growth (4). These models are based on thermodynamic balances involving surface and interfacial energies and stresses built up in the films and have been discussed in detail previously (5–7). For homoepitaxy, i.e. the deposition of a material onto itself to form a single crystalline film over the original surface, the growth should proceed via the FM process in the thermodynamic limit. An important realization is that for heteroepitaxy, i.e. the deposition of one material onto a different material, there are thermodynamic driving forces (the Grinfield instability) that will roughen the surface through the growth of separate islands (8). The applicability of the paradigm depends on the attainment of local equilibrium on the growing surface, which requires that the mass transport processes parallel to the surface be fast compared to the flux of depositing or etching species arriving at the surface. In modern technological applications, however, the drive is toward lower substrate temperatures to minimize unwanted chemical interactions within a complex material system and higher growth rates to achieve more economical production (9). These factors push practical deposition of films by vapor-phase processes away from the idealized thermodynamic limits and toward a nonequilibrium or kinetically limited regime. At the same time, the requirements with respect to minimizing surface roughness have become even more stringent.

The influence of kinetics on surface topology was experimentally recognized when chemical analyses by Auger spectroscopy and other surface-sensitive techniques indicated that the three thermodynamic models discussed above did not explain the morphology of many deposited films (10). New models involving the growth of pyramidal shaped islands, i.e. simultaneous multilayers, which form when the deposition rate is high compared to the lateral mass transport rate, were then proposed (11). The dependence of surface morphology on incident flux for material deposition is illustrated in Figure 2, and this has also been the object of theoretical investigation for decades (12–14). At low fluxes, the atoms or molecules that arrive on a surface will diffuse with a low probability of encountering other deposited species. These diffusing species eventually arrive at a step edge and are incorporated into the growing film. This is the process of step-flow growth, which is generally considered to produce the flattest possible surfaces and is the kinetic route to achieve FM films (15–17). At higher incident fluxes, the probability that two or more diffusing species will contact increases as R^m, where R is the flux and m is the number of species fusing together. If m is the critical number required to nucleate an island, then the area density of nuclei is extremely sensitive to the kinetics

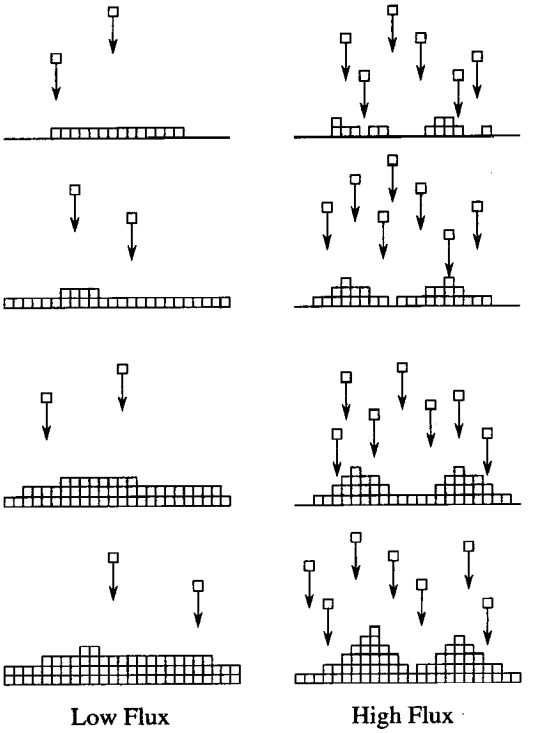

Figure 2 Illustration of the influence of incident flux on the morphology of a growing surface. At low flux, very little interaction occurs between adsorbed species before they diffuse to step edges and stick, thereby leading to step edge growth and relatively flat surfaces. At high fluxes, the probability of several adsorbed species coming together to form the nucleus of an island is much greater, and the result is the growth of simultaneous multilayers that form many islands and produce roughening of the surface.

of growth. At high enough fluxes or low enough substrate temperatures, islands nucleate on top of other islands, and the growth of a rough surface with pyramidal shaped features proceeds regardless of the thermodynamically most favored structure for the film (11, 12, 18, 19).

With the introduction of high-resolution electron microscopies and scanning probe techniques such as scanning tunneling microscopy (STM) and atomic force microscopy (AFM), actual pictures of the various stages of film growth have been obtained (20). The pictures seldom resemble either the quasithermodynamic ideals of stable film structures with locally flat surfaces or the kinetic models with pyramids, as shown in Figure 3. These examples are all for the heteroepitaxial deposition of thin films of CuCl on a lattice-matched CaF_2 substrate (21), but qualitatively similar

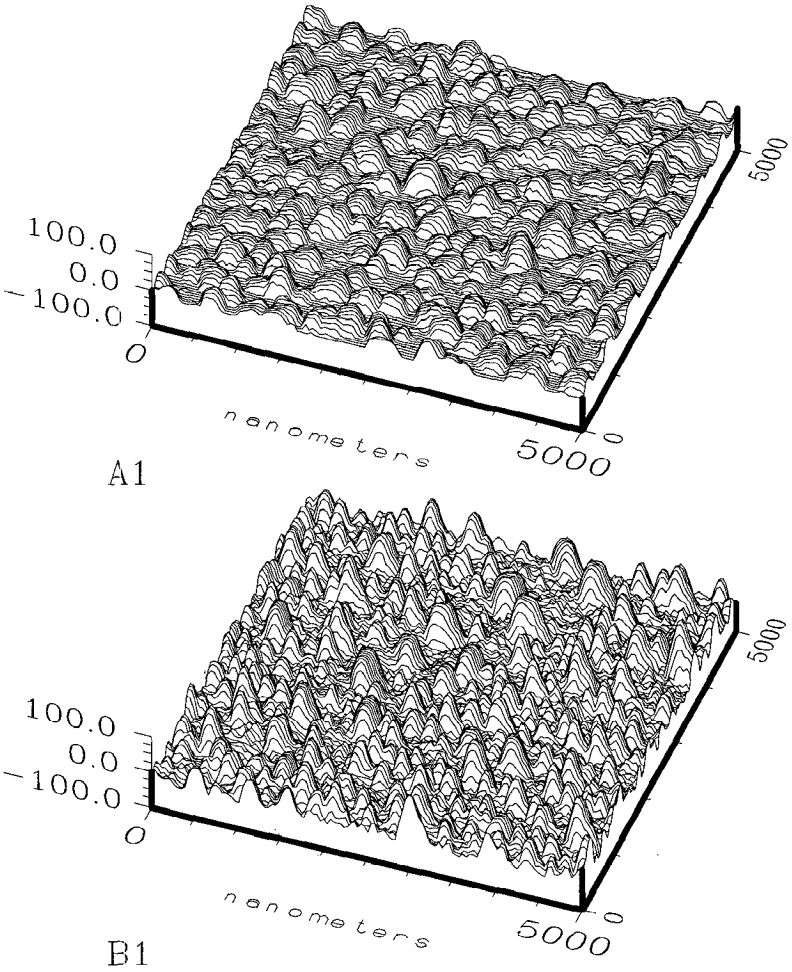

Figure 3 Topographs of epitaxial CuCl films grown on CaF_2 (111) substrates (21). The z-scale is expanded by 5× compared to the x-y scales. Two different growth temperatures and two different deposition fluences are shown: A is 110°C, B is 80°C, 1 is 6 nm, and 2 is 12 nm (*continued on next page*).

images have been obtained for a wide range of growth processes involving the deposition or etching of single crystalline, polycrystalline, and amorphous materials. The complexity of the morphology presents significant challenges to characterize the type, amount, and temporal evolution of the topography of a growing surface quantitatively.

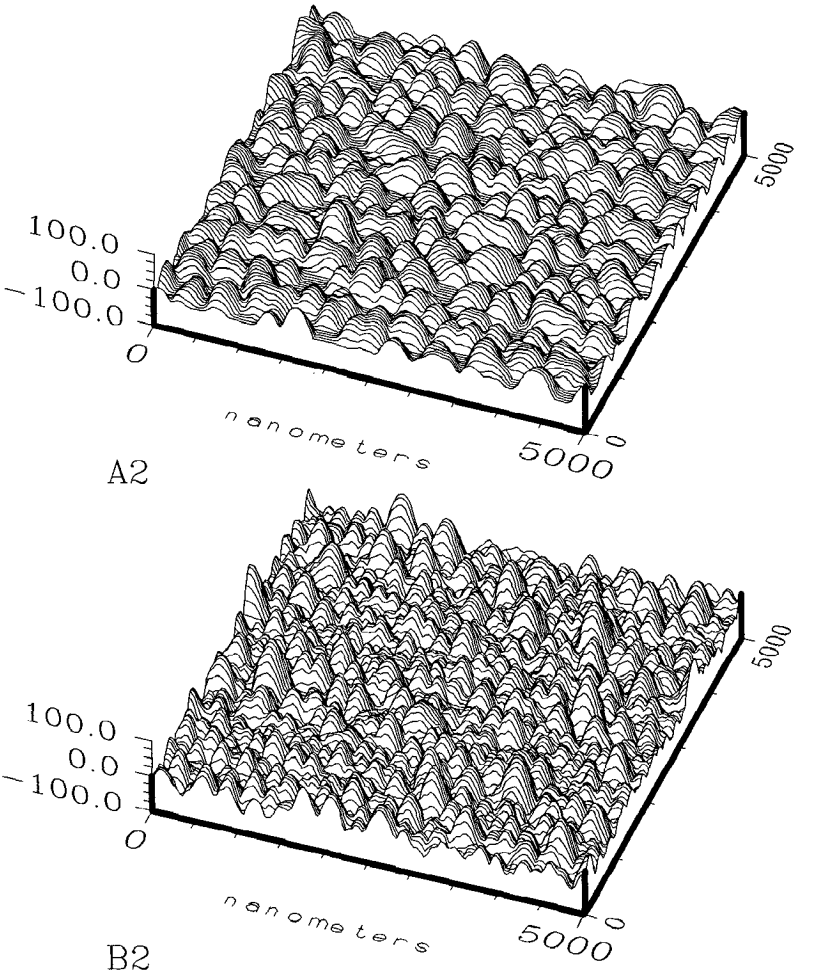

Figure 3—(continued)

PHENOMENOLOGY

Stochastic Roughening and Gaussian Smoothening

The extreme kinetic limit of growth via a surface-vapor interaction is the stochastic addition or removal of atoms with no lateral transport on the surface. Figure 4 illustrates the growth of a surface by the random deposition of 10, 100, and 300 monolayers of atoms onto a 64×64 square lattice, or by holding the figure upside down, the random withdrawal of

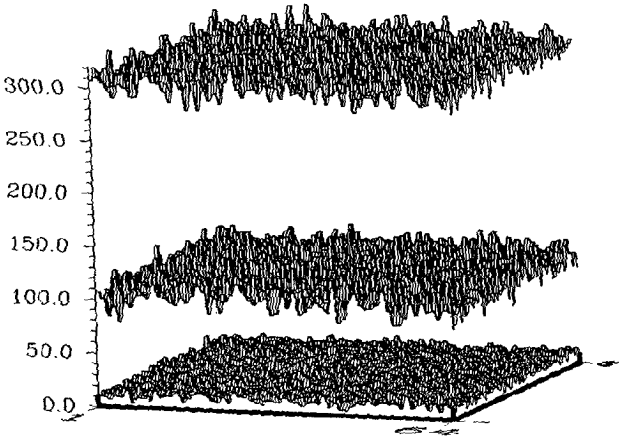

Figure 4 Stochastic surface growth on a 64 × 64 segment of a square lattice for the deposition of 10, 100, and 300 monolayers. The z-scale is contracted by 1/5× compared to the x-y scales.

atoms. In this illustration, the atoms only come to rest when they have touched the next highest atom on a lattice site; thus, no overhangs or internal voids in the film are possible. Such structures are observed in real films and more realistic simulations (22, 23), but this simple picture is presented here to introduce the methods for quantitatively characterizing a rough surface rather than as a model of how real surfaces grow. As growth proceeds, the roughness of the surface increases, and the noise level essentially follows a Poisson distribution in which the standard deviation is proportional to the square root of the amount of material deposited, $|\langle S(\boldsymbol{r})\rangle|^{1/2}$, where the triangular brackets indicate an average over $\boldsymbol{r}$. The primary feature of this stochastic model is that there is no correlation at all in the heights at different locations on the surface.

Of course, a totally random surface is not physically possible because some lateral transport of the atoms will always smoothen the roughness. The simplest way to model such a smoothening is to convolute a stochastic surface with a two-dimensional Gaussian function, as illustrated in Figure 5. Here, the rough surface of the 300-monolayer stochastic film in Figure 4 has been convoluted with a symmetric two-dimensional Gaussian, $\Gamma(|\boldsymbol{r}|) = 1/(\pi\sigma^2)\exp(-|\boldsymbol{r}|^2/\sigma^2)$, where σ, the lateral correlation length, is 2 or 4 atomic diameters and $|\boldsymbol{r}|$ is the magnitude of the vector $\boldsymbol{r}$. These surfaces look qualitatively similar to those in Figure 4 and many others that are

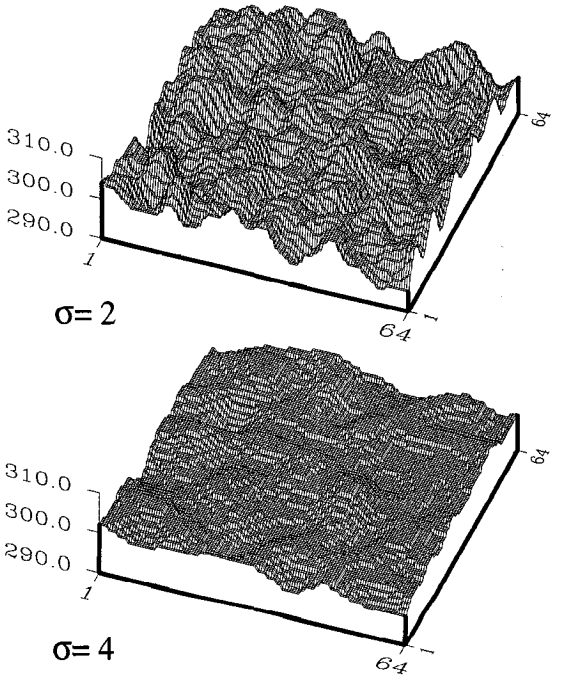

Figure 5 The stochastic surface for 300-monolayer deposition after convolution with a two-dimensional Gaussian function that has a correlation length corresponding to 2 and 4 atomic diameters. The z-scales are different from those in Figure 4.

produced by deposition or etching, but a quantitative method of analyzing surface morphology is required to allow comparison of rough surfaces with each other and with different models to describe the roughness. The growing surface in the comoving frame of reference, which is the experimental observable, is defined to be $H(\mathbf{r}) \equiv S(\mathbf{r}) - \langle S(\mathbf{r}) \rangle$. The most obvious quantitative characteristic of a rough surface is the root-mean square (rms) of $H(\mathbf{r})$ or the standard deviation of the surface height, $\delta \equiv [\langle H(\mathbf{r})^2 \rangle]^{1/2}$. This is an important number for characterizing variations perpendicular to the average surface, but many investigators have focused too narrowly on just this one parameter. The concept of roughness also involves the aspect ratio of the height to the width of the features or the corrugation of the surface. For a given value of δ, the surface with the largest aspect ratio is usually considered to be the roughest. Thus, a measurement of the extent of features in the plane of growth, i.e. the lateral correlation length, is also required to describe a surface.

Autocovariance and Spectral Power Density

Quantitative information about both the height variations and the lateral correlation is provided by the autocovariance function (24–26),

$$G(|\boldsymbol{r}|) \equiv \langle H(\boldsymbol{r}')H(\boldsymbol{r}'-\boldsymbol{r})\rangle - \langle H(\boldsymbol{r})\rangle^2 = \langle H(\boldsymbol{r}')H(\boldsymbol{r}'-\boldsymbol{r})\rangle, \quad 1.$$

where the surface roughness is assumed to be isotropic here so that G is a function of the magnitude of $\boldsymbol{r}$. At $|\boldsymbol{r}| = 0$, $G(0)$ is the variance δ^2 of the surface height, but the behavior of $G(|\boldsymbol{r}|)$ for $|\boldsymbol{r}| > 0$ represents a quantitative description of how the heights at different points on a surface are correlated to each other as a function of their separation $|\boldsymbol{r}|$. Calculating $G(|\boldsymbol{r}|)$ of a surface is a way to compress a data set enormously, since the $n \times n$ triples of numbers (H, x, y) that represent topographic information in three dimensions are compressed into a two-dimensional representation with only n pairs of numbers $(G, |\boldsymbol{r}|)$. This may represent a reduction in the number of experimental data points to be considered and processed mentally by several orders of magnitude, and at the same time $G(|\boldsymbol{r}|)$ can reveal details hidden in the complexity of a topograph. The $G(|\boldsymbol{r}|)$ for the random surface of Figure 4 resembles a delta function because $G(0)$ is the variance of the surface but $G(|\boldsymbol{r}|) \approx 0$ for $|\boldsymbol{r}| > 0$. This is the quantitative statement that the heights at different locations on the stochastic surface are uncorrelated. On the other hand, the autocovariance functions for the smoothened surfaces from Figure 5 have a width determined by the lateral correlation length, σ, used in smoothening the stochastic surface, as shown in Figure 6*a*. Thus, because the autocovariance function can be computed for any r by (25)

$$G(|\boldsymbol{r}|) \approx \delta^2 \exp(-|\boldsymbol{r}|^2/\sigma^2), \quad 2.$$

a Gaussian model of roughness allows the surface morphology to be characterized by only two numbers: the standard deviation of the surface height δ and the lateral correlation length σ. Determining δ and σ represents an extremely significant data compression as only two numbers quantitatively characterize an entire $n \times n$ topograph in three dimensions.

Another convenient data summarization function is the spectral power density or the structure factor for the rough surface (27),

$$g(|\boldsymbol{q}|) \equiv \mathcal{F}[G(|\boldsymbol{r}|)], \quad 3.$$

where $\mathcal{F}$ is the two-dimensional Fourier transform operator. The spectral power density is an extremely useful function because the electrooptical (28) and chemical properties (8) of a rough surface can be formulated in terms of $g(|\boldsymbol{q}|)$. Figure 6*b* shows the spectral power densities for the stochastic model and the smoothened surfaces of Figure 6*a*. The spectral

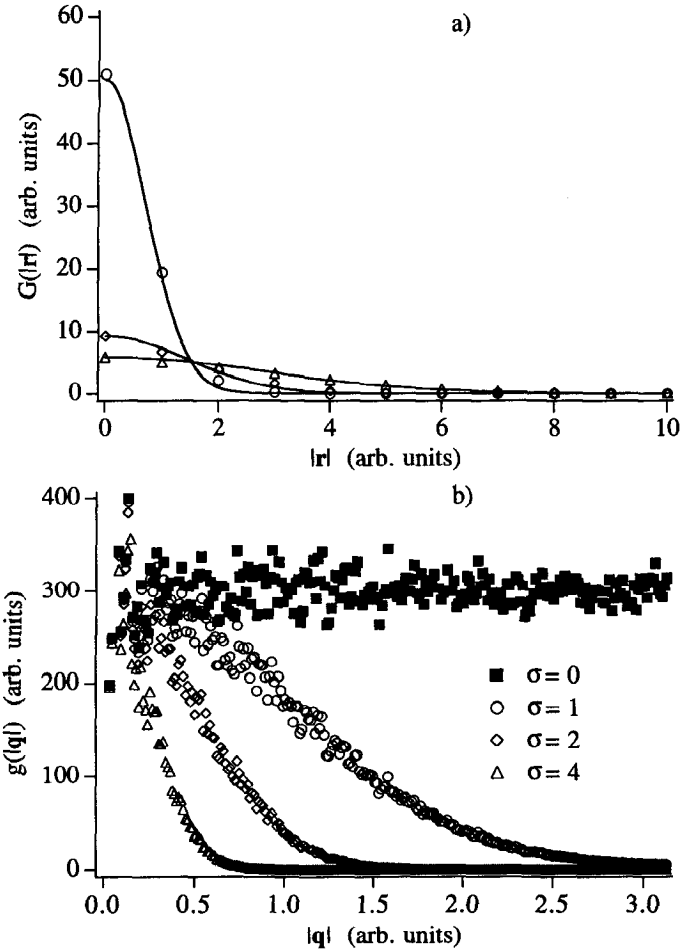

Figure 6 (*a*) The autocorrelation function $G(|\boldsymbol{r}|)$ computed for the three Gaussian-smoothened surfaces from Figure 5. The corresponding autocorrelation function for the original stochastic surface of Figure 4 on this scale is $G(0) = 300$ and $G(|\boldsymbol{r}|) = 0$ for $|\boldsymbol{r}| > 0$, and is not plotted because of the large difference in scale. (*b*) The corresponding reciprocal space spectral density $g(q)$ for the stochastic and the Gaussian-smoothened surfaces.

power density for the stochastic surface is essentially a constant, with a significant noise level because of the finite number (512×512) of data points sampled. The random arrival of depositing species roughens a surface the same amount at all length scales, thus producing features on the surface that are equal in magnitude at all wavenumbers. Because the

Fourier transform of a convolution of two functions is just the product of their Fourier transforms, $g(q)$ of the Gaussian-smoothened surfaces is (25)

$$g(|\boldsymbol{q}|) \approx \pi\delta^2\sigma^2 \exp\left(-\frac{\sigma^2|\boldsymbol{q}|^2}{4}\right). \qquad 4.$$

The obvious route of obtaining δ and σ for a particular surface is by computing the autocorrelation function from real-space data and then fitting $G(r)$ to a Gaussian (24, 26). However, a reciprocal-space experiment that may be used to ascertain the rms roughness and the correlation length of a surface is to determine $g(q)$ by measuring the angle dependence of the nonspecular intensity in a light-scattering experiment (29, 30). In a plot of $\ln[g(|\boldsymbol{q}|)]$ vs $|\boldsymbol{q}|^2$, the slope yields $-\sigma^2/4$ and the value of $\ln[g(|\boldsymbol{q}|)]$ extrapolated to $|\boldsymbol{q}| = 0$ yields $g(0) = \pi\delta^2\sigma^2$. This method has been shown to be quite sensitive. Before real-space techniques had sufficient resolution, values of δ as small as a few angstroms had been inferred (31) from the scattering of visible radiation from rough surfaces by assuming that the experimental spectral density has the functional form of Equation 4.

Early Experimental Observations

Because of the technological importance of mirrors, the surface roughness of metal films deposited onto various types of optical flats has been measured using several different techniques (25, 25a). Very often, the characterization of these surfaces yielded results that differed significantly from the expectations of Equations 2 and 4. The experimentally determined autocorrelation functions for an example of heterodeposition, e.g. Ag thin films grown on insulating substrates, are shown in Figure 7. These data were obtained by digitizing real-space images of deposited Ag films obtained with an electron microscope, which requires a means to calibrate the z-scale of the resulting topographs (25, 32). The autocorrelation functions display statistically significant oscillations about $G(|\boldsymbol{r}|) = 0$, and thus cannot be modeled by a simple Gaussian function as in Equation 2. One approach to improve the model for $G(|\boldsymbol{r}|)$ is to fit the experimental data to a somewhat more complex function (25),

$$G(|\boldsymbol{r}|) \approx \delta^2 \exp(-|\boldsymbol{r}|^2/\sigma^2)\cos(b|\boldsymbol{r}|), \qquad 5.$$

where the cosine term is used to model the oscillations in the experimental data. This adds a third number, b, to the set often used to quantitatively characterize a rough surface. The physical meaning of this additional number is actually more clear when considering the Fourier transform of Equation 5,

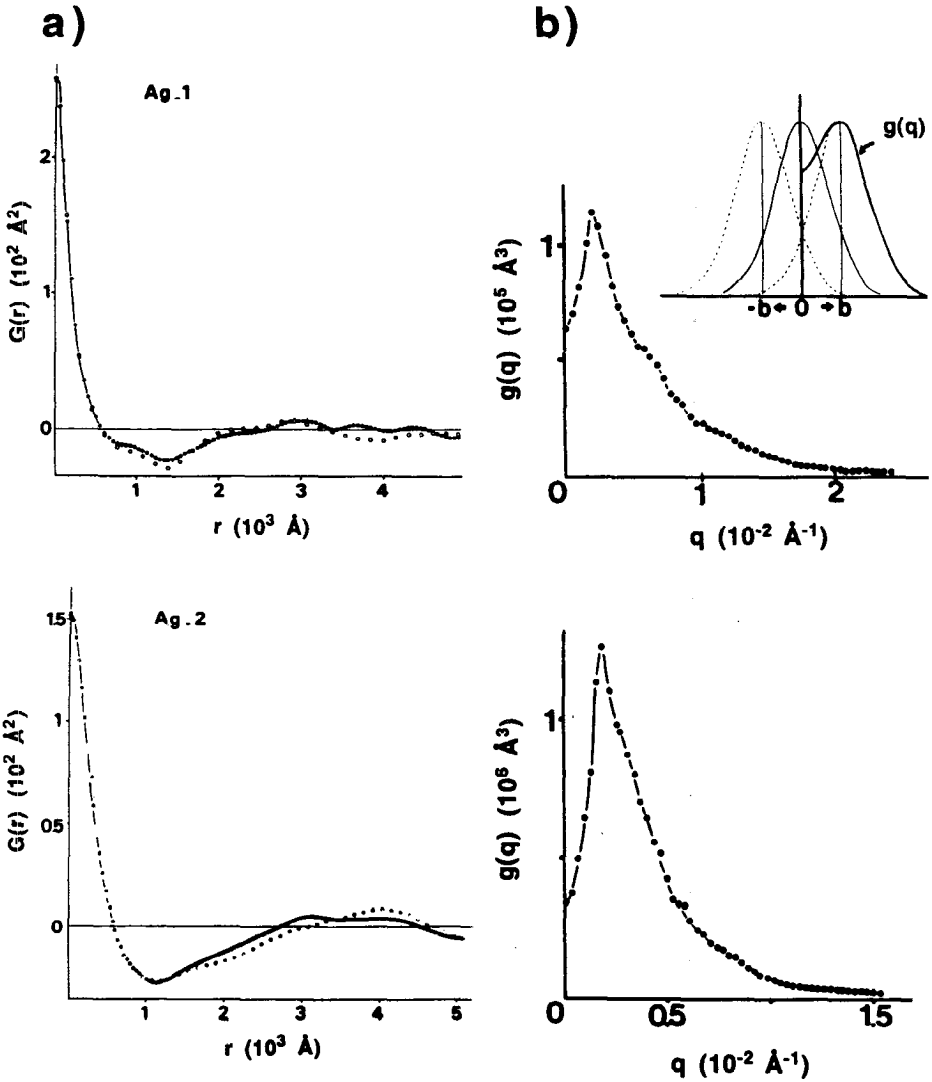

Figure 7 (*a*) Experimentally determined autocorrelation functions for silver films deposited onto insulating substrates (25). These functions display the oscillations about $G(|\boldsymbol{r}|) = 0$ that represent typical behavior for the autocorrelation functions of surface growth. (*b*) The spectral density functions for the same data as (*a*). There is a pronounced peak in the spectral density for $\boldsymbol{q} > 0$. The inset in (*b*) shows how the spectral density is modeled in Equation 6 by shifting the peak of a Gaussian distribution up to $|\boldsymbol{q}| = b$ to correspond with the peak in the experimental distribution.

$$g(|\boldsymbol{q}|) \approx (\pi/2)\delta^2\sigma^2 \{\exp[-\sigma^2(|\boldsymbol{q}|+b)^2/4]+\exp[-\sigma^2(|\boldsymbol{q}|-b)^2/4]\}. \quad 6.$$

Thus, the peak in the reciprocal-space spectral density for heterodeposition of metals on insulators occurs at a nonzero spatial frequency $|\boldsymbol{q}| = b$, as shown in the examples of Figure 7*b* (25).

Equation 6 illustrates a major problem with the traditional analysis of experimentally measured spectral density functions obtained from a light-scattering experiment. Such data are necessarily collected over a finite range of $|\boldsymbol{q}|$, and usually do not include data close to $|\boldsymbol{q}| = 0$ because of the strong specular scattering of the incident light, which has some angular divergence. Obtaining a reliable value of δ from light-scattering experiments becomes very questionable if the peak in the spectral density occurs at $|\boldsymbol{q}| > 0$ for the actual distribution (25). If the data are analyzed according to Equation 4, the extrapolation of the experimental $\ln[g(|\boldsymbol{q}|)]$ to $|\boldsymbol{q}| = 0$ will yield a significant overestimate of the actual surface rms height. Thus, real-space imaging techniques will generally yield superior information about δ as long as they have a resolution that is significantly smaller than the lateral correlation length of the sample. The correlation length is often overlooked in analyses of rough surfaces, but in principle, σ can be easily determined from scattering measurements and can even be determined readily as a function of time by performing scattering experiments during surface growth.

Recently, autoregressive techniques have been adapted to characterize $G(|\boldsymbol{r}|)$ and $g(|\boldsymbol{q}|)$ from rough surfaces (33). This approach has been utilized because experimental data are often not satisfactorily modeled even by the three parameters: δ, σ, and b. Rather than extend the model of Equations 5 and 6 by adding higher-order moments and harmonics, which would not have a convenient physical interpretation, an entirely different parameterization has been proposed by Rasigni et al (33). In the autoregressive approach, the experimental spectral density function is approximated by a function of the form

$$g(|\boldsymbol{q}|) \approx g(0)|1+\Sigma a_n \exp(-i2\pi n|\boldsymbol{q}|\Delta x)|^{-2}, \quad 7.$$

where the a_n are fitting parameters and Δx is the characteristic spatial interval used in collecting real-space data. This form for the spectral density function fits the experimental data for Ag films deposited onto insulating substrates reasonably well if Equation 7 is taken up to the fourth order, as shown in Figure 8. This parameterization of $g(|\boldsymbol{q}|)$ is very useful if one requires a reasonably faithful representation of the entire spectral density function for numerical analysis of other properties of the rough surface. However, the coefficients a_n are not intrinsic properties of the surface, but rather depend on how the surface roughness data were

collected, i.e. on the spacing between measurements Δx. The coefficients a_n do not represent a convenient data compression for quantitative comparison of different surfaces with each other or with theory because no physical meaning can be associated with them.

Deficiencies

The parameters δ, σ, and b are phenomenological because they describe the rms surface height, the correlation length in the surface plane, and the spatial frequency of the maximum spectral density, but they give no insight into how or why a particular surface has formed the way it has. The values of δ, σ, and b determined at a given time do not provide any information about the evolution of a growing surface, and thus all three must be measured as functions of time to determine the temporal behavior of growth. In addition, a Gaussian appears to be too strong a smoothening function to model the lateral mass transport on a stochastically roughened surface because experimentally measured autocorrelation functions such as those in Figure 7*b* have values of δ and σ significantly larger than the models for Gaussian smoothened stochastic surfaces in Figure 6. In order to gain experimental control of the morphology of a growing surface, better models of surface roughness and an improved understanding of the growth process are required.

SCALING

Self-Affinity and Self-Similarity

Another approach to the understanding of surface growth employs the concept of topographical scaling (34). The most familiar type of scaling is self-similarity, which itself is a restricted case of a more general class, self-affinity. If $\kappa H(\kappa \boldsymbol{r})$ is indistinguishable from $H(\boldsymbol{r})$, then H is *self-similar*, but if the z-axis must be multiplied by a different factor, i.e. $\kappa' H(\kappa \boldsymbol{r})$ is indistinguishable from $H(\boldsymbol{r})$, then H is *self-affine*. Many real surfaces appear to be self-affine over a restricted range of length scales (32, 35, 36), and this observation has stimulated the application of fractal geometry to the study of surface growth (37–39).

The patterns that form during the growth of surfaces are similar for very different materials and over many orders of magnitude in film thickness for the case of deposition. Different communities of researchers have discovered the fractal-like nature of these patterns and have developed quantitative means for analyzing the structure and understanding the origins of the patterns, often in complete isolation from one another. Examples of these analyses range from the condensation of water vapor on cold glass surfaces (breath figures) (40–44) to the ion bombardment

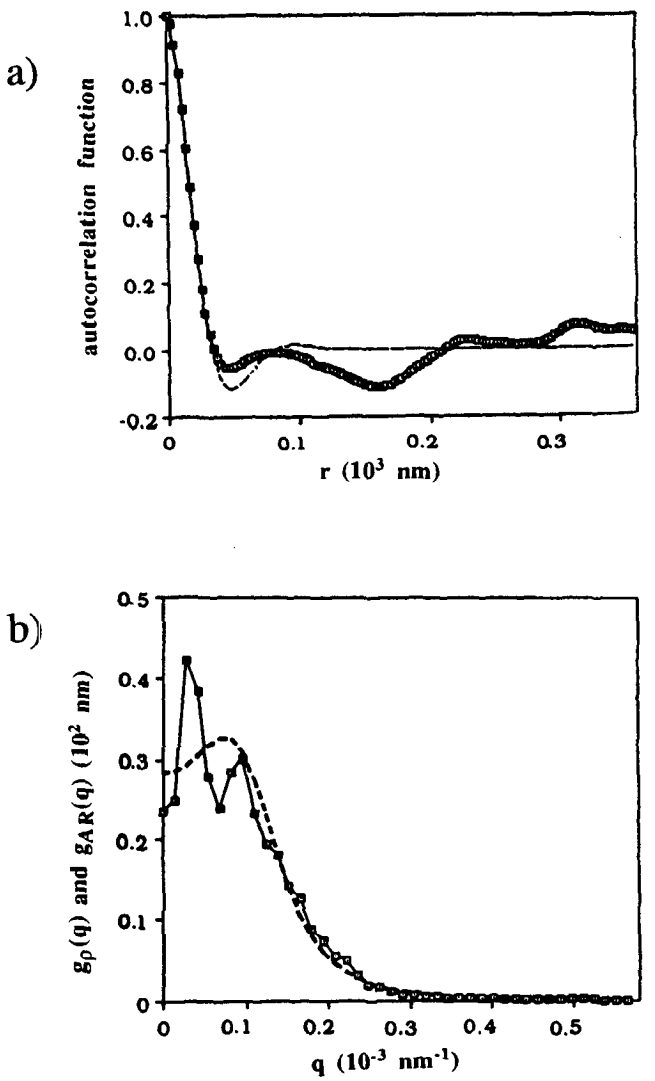

Figure 8 (*a*) An autoregressive fit to the experimental autocovariance function for a thin metal film deposited onto an insulating substrate (33). (*b*) The autoregressive fit to the spectral density corresponding to (*a*).

erosion of solid surfaces (22, 45–49). Scaling analyses have been developed for many types of geometries and dimensions, including growth of a one-dimensional surface (1+1D), nucleation and growth confined to a plane (2D), growth perpendicular to a plane (2+1D), and higher dimensional systems (37, 50, 51). Even within a particular dimensionality, different viewpoints of the basic building blocks of the surface can be adopted, such as aggregates of different-sized spherical droplets that can display some mobility and coalescence or identical cubes that can be transported about the surface until they come to rest at a favorable position. Describing and comparing all these approaches is beyond the scope of this review. Here, we consider only one scaling approach and refer interested readers to some of the many reviews for details of alternate formulations (37, 38, 50).

Scaling of the Interface Width in 2+1D

In 1985, Family & Vicsek (52) analyzed the behavior of growing surfaces by assuming that they were self-affine. They showed that the standard deviation of the surface height ξ_L, also called the interface width, of a growing self-affine surface can be expressed in the form (16)

$$\xi(L, t) = L^{\alpha} f(t/L^{z}), \qquad 8.1$$

where $f(x)$ is a function that behaves as x^{β} for $x \ll 1$ and as a constant for $x \gg 1$. This reduces to

$$\xi(L, t) \sim t^{\beta} \quad \text{for} \quad t/L^{z} \ll 1 \qquad 8.2$$

and to

$$\xi(L, t) \sim L^{\alpha} \quad \text{for} \quad t/L^{z} \gg 1, \qquad 8.3$$

where L is the length scale over which the roughness is measured and t is the elapsed time of growth, which is usually proportional to the amount of material deposited (or removed). The two new parameters α and β are called the static (or spatial) and dynamic (or temporal) scaling exponents, respectively, and z is α/β.

As illustrated in Figure 9, the rms roughness of a surface is actually a function of the length scale L over which it is measured until the roughness saturates at some critical length L_c, above which $\xi_L = \delta$ because a finite amount of material has been deposited. For a self-affine surface, a plot of ξ_L vs L on a log-log scale yields a straight line with slope $0 < \alpha < 1$ for $L \leq L_c$; for a self-similar surface, $\alpha = 1$. The interface width as a function of length scale is related to the autocorrelation function in the following fashion (53, 54):

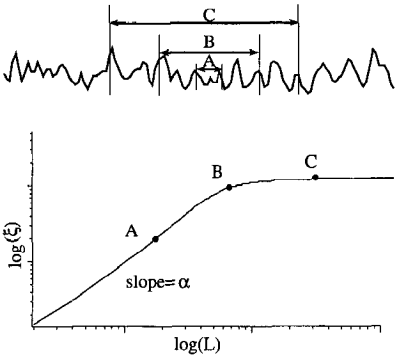

Figure 9 An illustration of the dependence of the interface width ξ on the length scale used to measure the surface roughness. At very small length scales, the apparent rms height is small, but the measured interface width increases as the length scale expands until it achieves a saturation value determined by the fact that the variations in the surface are finite.

$$\xi_L^2 = \left(\frac{1}{L^2}\right)\int_0^L [\delta^2 - G(r)]r\,\mathrm{d}r. \qquad 9.$$

Thus, by approximating the log-log plot of Figure 9 with a pair of straight line segments to depict the behavior of $\xi(L)$, an approximation for the autocorrelation function for a self-affine surface with spatial scaling exponent α is

$$G(r) \approx \begin{cases} \delta^2\left[1 - \dfrac{\alpha+1}{2}\left(\dfrac{r}{L_c}\right)^{2\alpha}\right], & \text{for} \quad r \le L_c \\ 0, & \text{for} \quad r > L_c, \end{cases} \qquad 10.$$

and is illustrated for $\alpha = 1$ in Figure 10*a*.

The Fourier transform of Equation 10 yields the spectral density function

$$g(|\boldsymbol{q}|) \approx \begin{cases} \dfrac{\alpha}{\pi}\delta^2 L_c^2, & \text{for} \quad |\boldsymbol{q}| < 1/L_c, \\ \dfrac{\alpha}{\pi}\dfrac{\delta^2}{L_c^{2\alpha}} q^{-2(\alpha+1)}, & \text{for} \quad |\boldsymbol{q}| \ge 1/L_c, \end{cases} \qquad 11.$$

as shown in Figure 10*b*. Thus, comparing Figures 6 and 10 shows that a self-affine surface has a qualitatively similar but quantitatively distinct geometry from a surface with Gaussian roughness. Comparing the two spectral density functions (Equations 4 and 11) at $|\boldsymbol{q}| = 0$ shows that

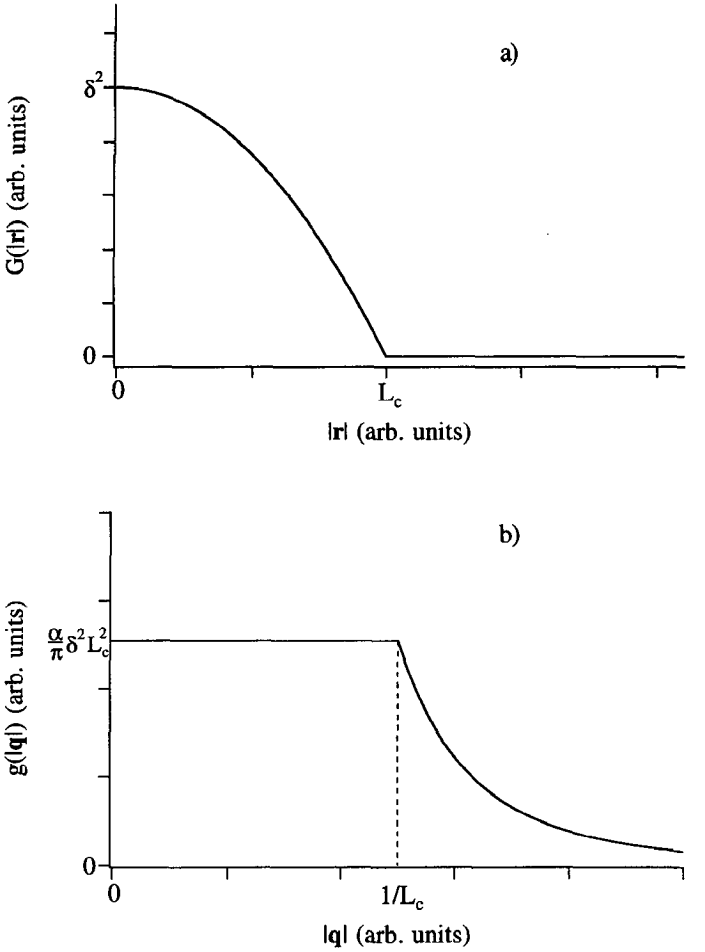

Figure 10 (*a*) The autocovariance function corresponding to the straight line segment model for the log-log plot of the interface width versus length scale for a self-similar surface. (*b*) The spectral density function for the same example as (*a*).

$L_c \approx [\pi/(\alpha)^{1/2}]\dot{\sigma}$, and thus the critical length for scaling L_c can also be viewed as the appropriate metric for the lateral correlation length for a self-affine surface.

The Family & Vicsek (52) analysis of a growing surface also explicitly considers the temporal behavior of the surface roughening. Plotting the log of the saturation value of ξ_L (i.e. δ) vs log (t) yields a straight line with a slope of β for a growing self-affine surface (inset of Figure 11). Thus, the

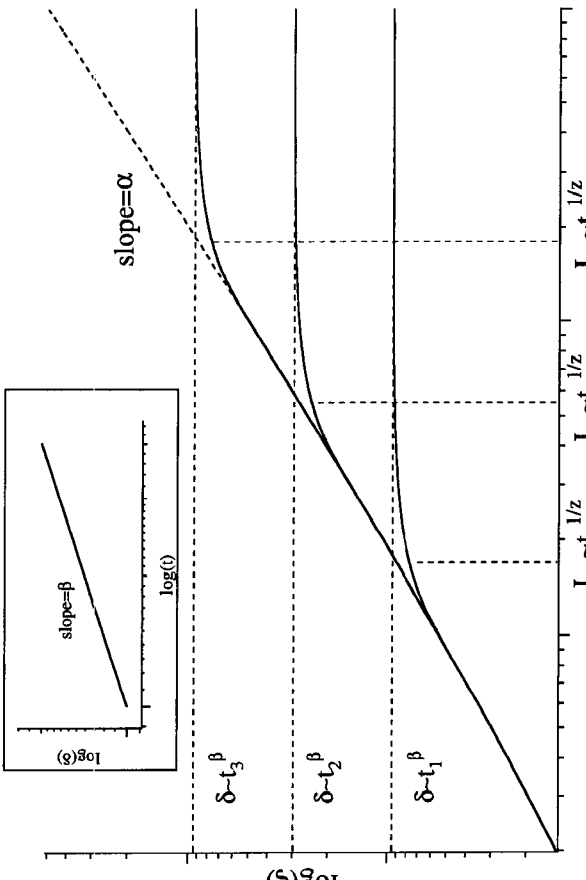

Figure 11 A schematic plot of the interface width of a self-similar surface as a function of length scale for several different growth times. The plateau in the ξ vs L curves defines the large scale value of the rms height δ, whereas the knee in the curves is the critical length L_c or the lateral correlation length for scaling. Both characteristic length scales increase with time. The inset shows a standard plot of $\log(\delta)$ vs $\log(t)$ used to determine the scaling exponent β.

time dependence of the surface rms is determined from Equation 8.2 ($\delta \sim t^{\beta}$) if β is known. Moreover, because the critical length for scaling and the deposition time are related to each other by $t/L_c^z \sim 1$ from Equations 8.2 and 8.3, the time dependence of the lateral correlation length is also known to be $L_c \sim t^{\beta/\alpha}$. Figure 11 shows how the temporal dependence of δ and L_c can be determined from the spatial and temporal dependence of ξ_L. If the growing surface is self-similar ($\alpha = 1$) at any time, then the correlation length and the surface rms have the same time dependence, and thus the surface will be self-similar at all times. However, if the surface is self-affine, then the correlation length of the surface must increase faster than the surface rms, and thus the ratio δ/L_c will decrease with time. The amplitude of the rms of a self-affine surface will increase, but the corrugation will decrease as the surface grows.

The parameters α and β provide a pair of numbers that can be used to classify the spatial and temporal scaling of growing surfaces quantitatively, and thereby identify the growth process according to its symmetry in a renormalization group sense. If the two system-dependent parameters δ and L_c are also known at some time τ, the surface rms and the correlation length can be predicted for all times during the growth of the surface:

$$\delta(t) = \delta(\tau)\left(\frac{t}{\tau}\right)^{\beta} \qquad 12.$$

and

$$L_c(t) = L_c(\tau)\left(\frac{t}{\tau}\right)^{\beta/\alpha}. \qquad 13.$$

Thus, if growing surfaces are truly self-affine, they can, in principle, be completely characterized in space and time by only five numbers: The scaling exponents should be universal and predictable from theory, whereas the surface rms and correlation length are system dependent and must be measured at least once for each particular set of growth conditions. In some cases predicted by theory (50, 55), additional constraints relate α and β, so that in fact the entire spatial and temporal evolution of a growing surface may be determined from only four independent parameters, which reveals a remarkable simplicity underlying the complex process of surface growth.

Continuum Equations of Motion

The scaling of growing self-affine surfaces arises from the competition between the stochastic roughening and various smoothening mechanisms.

One way to analyze the scaling behavior for various models of growth is through numerical simulations with Monte Carlo or molecular dynamics techniques, and such analyses have yielded important insights (37, 41, 50, 56, 57). However, the amount of computer time required to simulate the evolution of many features on a surface that are hundreds of atomic diameters high and thousands in width for a 2+1D system ($>10^9$ atoms) is well beyond present computer technology. Because such sizes are common for actual surfaces, many investigators have developed continuum models that represent the equation of motion of a growing surface and then analyzed the behavior of such equations after they have been spatially averaged in order to predict the scaling exponents.

The simplest model of the evolution of surface morphology by deposition or etching involves only the white noise present in the flux of the incident species, as represented in Figure 5. A continuum equation of motion that models this stochastic growth is (37)

$$\frac{\partial H(\boldsymbol{r}, t)}{\partial t} = \eta(\boldsymbol{r}, t), \qquad 14.$$

where $\eta(\boldsymbol{r}, t)$ is a function (50) that produces a Poisson distribution with a mean equal to the total amount of material deposited or removed. The spatial scaling exponent $\alpha = 0$ for the stochastic surface produced by Equation 14 because the surface is completely random, and thus the value of ξ_L^2 will be independent of the length scale used to measure it. An alternate way to think of the stochastic limit is that $L_c = 0$. The temporal scaling exponent $\beta = 1/2$ because the standard deviation for a stochastic process is proportional to the square root of the amount of material deposited or removed and, thus, the time t, if the incident flux of depositing material or etchant is constant. In this limit, an initially flat surface will become continually rougher as time proceeds, but the correlation length will always be zero, just as in the discrete examples of Figure 5.

In 1986, Kardar, Parisi & Zhang (KPZ) (58) proposed an equation of motion intended to describe the spatial and temporal evolution of a nonequilibrium growing surface:

$$\frac{\partial H(\boldsymbol{r}, t)}{\partial t} = \nu \nabla^2 H + \frac{\lambda}{2}(\nabla H)^2 + \eta(\boldsymbol{r}, t). \qquad 15.$$

This KPZ equation was derived from arguments of simplicity and symmetry rather than on any mathematical representation of the physical mechanisms of surface growth (and therefore its exact physical interpretation has been a subject of discussion). The $\nabla^2 H$ term is the lowest-order derivative that would model the erosion of hills and the filling-in of valleys,

because it is negative for local maxima and positive for local minima. The $(\nabla H)^2$ term accounts for the nonlinearity assumed to be present in all physical systems and was chosen because it ensures that Equation 15 has rotational invariance, i.e. it is symmetric for small rotations about axes contained in the surface plane. Both ν and λ are system-dependent parameters. For the limit in which $\lambda = 0$, the KPZ equation reduces to the Edwards-Wilkinson (EW) Langevin equation (59), which has an analytical solution in 2+1D. In this case, there is only a logarithmic relation between ξ_L^2 and L, and thus $\alpha = 0$ and $\beta = 0$. The correlation length L_c is finite, as contrasted with the case of $\alpha = 0$ and $L_c = 0$ for the stochastic surface. Growth for which $\alpha = \beta = 0$ apparently corresponds to the Franck–van der Merwe model discussed above, in that an initially flat surface grows without significant roughening and thus establishes a link between the earlier thermodynamic and scaling ideas of surface growth. If $\lambda \neq 0$, the KPZ equation does not have an analytical solution and, therefore, must be examined either through renormalization group theory or numerical simulations. Several studies have shown that the presence of the nonlinear term in the KPZ equation causes both the scaling exponents to increase to $\alpha \approx 0.4$ and $\beta \approx 0.25$, which in fact satisfy the relation $\alpha + \alpha/\beta = 2$ expected for a system with rotational invariance (37).

The KPZ equation has attracted a great deal of attention because it was initially thought to be a universal equation of surface growth independent of scale or mechanism. According to KPZ, for any system at long enough times, the nonlinear term in the equation of motion should eventually dominate the growth. One consequence of this postulate is that it should be impossible to grow a flat surface by a vapor-solid interaction under any circumstances, since both the scaling exponents for KPZ are nonzero. However, a great deal of empirical evidence that flat surfaces can be grown has accumulated from the epitaxial growth of metal and semiconductor surfaces (9, 60), which demonstrates that KPZ is not universal and that there are growth conditions under which the nonlinear term in Equation 15 may be negligible. In fact, careful measurements of α and β for many growing surfaces have shown that few physical systems actually conform to the detailed scaling predictions of KPZ, as will be illustrated below.

Several researchers have used the KPZ approach to propose and analyze alternate continuum equations of motion (61–74). Wolf & Villain (WV) (72) presented thermodynamic arguments to show that a $-\nabla^4 H$ term would better model the process of smoothening by surface diffusion, which is often considered to be the primary lateral mass transport mechanism in surface growth. They proposed the WV equation

$$\frac{\partial H(\mathbf{r}, t)}{\partial t} = -\omega \nabla^4 H + \eta(\mathbf{r}, t), \qquad 16.$$

which is linear and thus can be solved exactly in 2+1D to yield growth exponents of $\alpha = 1$ and $\beta = 1/4$, as a better alternative to model surface growth. Interesting consequences of this equation are that a growing surface will be self-similar and it will be impossible to grow a flat surface, if stochastic roughening and surface diffusion are the only processes contributing to the formation of surface morphology. Because $\alpha = 1$, the ratio of δ/L_c will be constant during the entire growth process, and thus, a WV surface can become significantly more corrugated than a KPZ surface for long growth times.

Given the importance associated with the nonlinear term in the KPZ equation, several researchers soon added such a term to the WV equation to yield (66, 70, 71)

$$\frac{\partial H(\mathbf{r}, t)}{\partial t} = -\omega\nabla^4 H + \rho\nabla^2(\nabla H)^2 + \eta(\mathbf{r}, t), \qquad 17.$$

which is characterized by the scaling exponents $\alpha = 2/3$ and $\beta = 1/5$. Villain (71) interpreted the nonlinear term as a model for the fact that steps can act as a source or sink of atoms on a growing surface, which means that Equation 17 may model step-flow and/or island nucleation growth. The continuum equations (15–17) are characterized by nearly the same small but nonzero temporal scaling exponent. Thus, the dependence of the surface rms on growth time is relatively weak in all three models, but δ must increase with time as the surface grows. The spatial scaling exponents differ considerably from each other, thereby providing a means to distinguish experimentally among the various scaling models. Equations 15 and 17 represent two different general classes of growth mechanism, and therefore, one can reasonably assume that many growing surfaces have an equation of motion that involves a linear combination of both. This can lead to more complex temporal and spatial behavior, such as a breakdown of scaling or kinetic phase transitions, as discussed by Villain (71).

Each model discussed above predicts distinct scaling that can be directly compared to experimental results through the exponents α and β. To date, most of the experimental investigations of the topological behavior of growing surfaces have been intended to determine the validity of the scaling ideas, primarily by testing if plots of $\log(\xi_L^2)$ vs $\log(L)$ and/or $\log(\delta)$ vs $\log(t)$ actually yield straight lines and if the scaling exponents determined from the experimental data are close to one of the model predictions. The primary techniques used in these recent studies to examine the spatial scaling are X-ray (53, 78–82) or electron (83, 84, 84a) scattering and to determine the temporal scaling are STM or AFM (21, 45, 53,

60, 75–77). These methods are complementary, because the real-space topographs are readily analyzed to yield α, but to obtain temporal information from STM or AFM requires the growth of an entire series of samples with the subsequent collection and analysis of a large number of topographs. X-ray and electron scattering can be performed as the samples are growing and thus provide real-time information on the surface roughness with which to determine β. However, determining the spectral density $g(\boldsymbol{q})$ over a large enough range of $\boldsymbol{q}$ to allow the determination of α from reciprocal space data is challenging (82, 83). Table 1 summarizes the predictions for the scaling exponents of the various theoretical models and presents some experimental values obtained from the literature.

Several issues arise in the comparisons of experimental and theoretical values of the scaling exponents. First, most of the reported values of α tend to cluster either around $\alpha \approx 0.7$ predicted by Equation 17 or around the value of $\alpha \approx 0$ for the flat semiconductor surfaces of MBE growth, and relatively few at the intermediate KPZ value of $\alpha \approx 0.4$. These observations indicate that surface diffusion certainly plays an important role in the development of surface morphology, but apparently some other mechanism is responsible for the extremely flat surfaces produced by high-temperature MBE growth. Also, rotational invariance is apparently not

Table 1 Theoretically predicted and experimentally observed values of α and β

	α	β	Reference
Continuum Models			
Stochastic roughening	0	$\frac{1}{2}$	Equation 14
Evaporation-recondensation	0	0	Equation 15, $\lambda = 0$
KPZ	$\sim$0.4	$\sim$0.25	Equation 15, $\lambda \neq 0$
Surface diffusion	1	$\frac{1}{4}$	Equation 16
Surface diffusion plus steps	$\frac{2}{3}$	$\frac{1}{5}$	Equation 17
Experimental Observations			
Ion etched SiO_2 films	NA[a]	1.0	89
Ion etched graphite	0.4	1.0	45
O atom etched graphite	0.71	0.6	76
Ion etched Fe films	0.53	NA	49
Vapor deposited Fe	0.79	0.22	83
Vapor deposited Au	0.73	NA	75
Vapor deposited Pt	0.68	NA	77
Sputter deposited Au	NA	0.40	53
MBE CuCl	0.85	NA	21
MBE GaAs	$<$0.2	$<$0.1	60

[a] NA—not available.

obeyed by most real growing surfaces because KPZ-like behavior is rare. The requirement for rotational invariance may be broken by the presence of crystal planes. Second, reported values of the temporal scaling exponent are either $\beta \approx 0$ for MBE growth or they are significantly larger than those predicted by any of the continuum theories. The value of β can even exceed 0.5, which is the value for a purely stochastic surface with no smoothening at all. This indicates that there are important roughening mechanisms contributing to the evolution of surface morphology in addition to stochastic noise that have not been considered in the scaling approaches.

An even more fundamental issue is that it may not be possible to determine scaling exponents for many growing surfaces. Inspection of the log-log plots of experimental ξ_L^2 vs L data, such as those in Figure 12 for CuCl films grown on CaF_2 substrates (21), shows that they are often not strictly linear over the range of data presented. It is usually not clear if these variations are the result of noise or other limitations in the measurements or of a breakdown in the assumption of scaling behavior. In fact, this method of data presentation is not very sensitive to deviations from scaling behavior because most functions plotted on a log-log scale over a restricted range of the independent variable will yield nearly straight lines. Because the autocorrelation function is related to the derivative of ξ_L^2 from Equation 9, it and the spectral density are much more sensitive to topological properties of rough surfaces, and therefore, they should represent the preferred method of data presentation and analysis (38). When spectral density functions are analyzed, it is clear that most experimental systems cannot be modeled very well by scaling relations. As illustrated in Figure 7*b*, a peak often occurs in the spectral density at some positive value of q (21, 25, 33), which from Equation 11 is a clear violation of scaling behavior. Thus, real growing surfaces are usually not self-affine, but the scaling models have provided valuable insight into the topology of growing surfaces and more importantly into the time dependence of growth.

MECHANISMS OF SURFACE GROWTH

Smoothening

The phenomenological view discussed in the previous section assumes all rough surfaces attain a single universal form; an alternative approach is to focus directly on the various roughening and smoothening mechanisms that affect surface morphology. Stochastic roughening is actually opposed by several different lateral mass transport processes that smoothen features on a surface. Herring (85) was the first to consider the evolution of features caused by four of these smoothening processes over 40 years ago in a scaling analysis of sintering. He derived simple kinetic expressions that

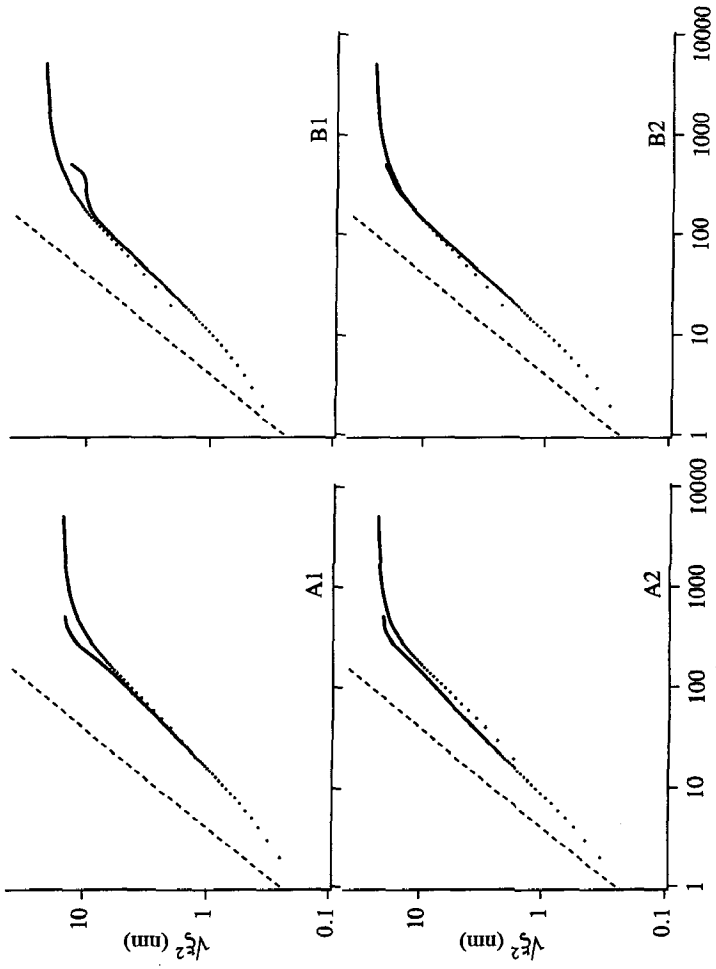

Figure 12 Plots of the logarithm of the interface width [log (ξ)] vs the logarithm of the length scale [log (L)] for the four CuCl on CaF_2 films shown in Figure 3.

governed the rate of change of a feature as a function of its size. The rate of smoothening can be described easily in reciprocal space by the expression (86)

$$\frac{\partial h(|\boldsymbol{q}|, t)}{\partial t} \propto -|\boldsymbol{q}|^n h(|\boldsymbol{q}|, t), \qquad 18.$$

where $\boldsymbol{q}$ is the wavevector, $h(|\boldsymbol{q}|, t)$ is the radial average of the Fourier transform of $H(\boldsymbol{r}, t)$, and n is 1, 2, 3, or 4, which represent the functional relationships for smoothening by plastic flow driven by surface tension, evaporation and recondensation of particles with different radii of curvature, volume diffusion, and surface diffusion, respectively. (Note: $n = 2$ has also been shown by Vvedensky et al (87) to correspond to a knock-off mechanism.) The derivation of the relationship between the smoothening mechanism of surface diffusion and the q-exponent $n = 4$ is an example of the scaling arguments used by Herring (85). Each smoothening mechanism affects the morphology differently and, thus, will leave a different signature in the spectral density function of the growing surface.

By combining the smoothening mechanisms with the stochastic roughening, an equation of motion in reciprocal space, which is essentially a kinetic rate equation, can be written for surface growth:

$$\frac{\partial h(|\boldsymbol{q}|, t)}{\partial t} \propto -c_n|\boldsymbol{q}|^n h(|\boldsymbol{q}|, t) + \eta(|\boldsymbol{q}|, t) \quad (n = 1 \text{ to } 4), \qquad 19.$$

where the first terms on the right model one of the smoothening mechanisms described by Herring (85), and the second term is the reciprocal-space stochastic noise term (the Fourier transform of the real-space term introduced in Equation 12) that describes the random arrival of the depositing species. The coefficients c_n can be expressed in terms of molecular-level properties of the system of interest (86). The noise term has the property

$$\langle \eta(\boldsymbol{q}', t')\eta(\boldsymbol{q}'', t'')\rangle = \delta(\boldsymbol{q}' - \boldsymbol{q}'')\delta(t' - t''), \qquad 20.$$

which represents the uncorrelated nature of the arrival of discrete depositing species (50). The expectation value of $|h(q, t)|^2$ can be determined analytically from Equation 19 if the surface is assumed to be flat at $t = 0$. This solution of Equation 19 is the radially averaged spectral power density (22, 25a, 59, 88):

$$g(|\boldsymbol{q}|, t) = \langle |h(|\boldsymbol{q}|, t)|^2\rangle = \Omega \frac{1 - \exp(-2c_n|\boldsymbol{q}|^n t)}{c_n|\boldsymbol{q}|^n}, \qquad 21.$$

where Ω is proportional to the flux, t is the deposition time, and c_n

(length^n · time^{-1}) is a constant characteristic of the specific lateral mass transport mechanism indicated by n. For all four values of n, smaller features (large q) are eroded away preferentially over large features (small q), but the q-dependence of the spectral density depends explicitly on the identity of the smoothening mechanism, as illustrated in the schematic log-log plots of Figure 13. At low values of q a flat plateau extends out to the critical spatial frequency $q_c = 1/L_c$, after which $\log[g(q)]$ vs $\log(q)$ decreases linearly with a slope of $-n$ because, at large q, Equation 21 approaches

$$g(|\boldsymbol{q}|, t) \propto \frac{\Omega}{c_n |\boldsymbol{q}|^n}. \qquad 22.$$

By comparing Equation 22 to Equation 11, a direct relation between the q-exponent n and the spatial scaling exponent α is revealed:

$$n = 2(\alpha + 1). \qquad 23.$$

Thus, as was already evident from the discussion of Equations 15–17, the value of the spatial scaling exponent depends on the smoothening mechanism. For the specific cases in which $n = 2$ and $n = 4$, Equation 21 is the spectral density function corresponding to Equation 15 without the

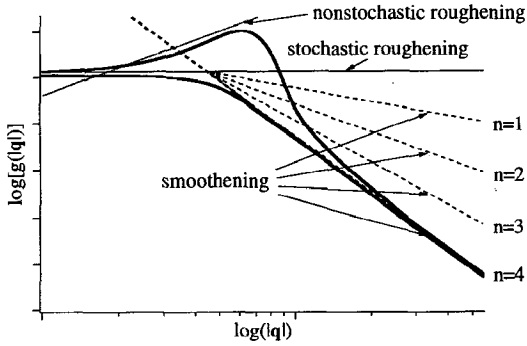

Figure 13 Schematic plots of the logarithm of power spectral density, $\log[g(|\boldsymbol{q}|)]$, vs the logarithm of spatial frequency, $\log(|\boldsymbol{q}|)$. Stochastic roughening by random deposition creates a surface that contains features of all sizes (*thin solid line*). The effect of the four smoothening mechanisms discussed by Herring (85), plastic flow ($n = 1$), evaporation-recondensation ($n = 2$), bulk diffusion ($n = 3$), and surface diffusion ($n = 4$), are plotted in dashed lines; the interplay between stochastic roughening by random deposition and smoothening by surface diffusion ($n = 4$) results in a $g(|\boldsymbol{q}|)$ that is depicted by the lower thick solid curve. Nonstochastic roughening by 3-D island formation also has a power dependence on $|\boldsymbol{q}|$ (*dotted line*). The net effect of nonstochastic roughening, stochastic roughening, and surface diffusion acting in concert is the creation of a peak in $g(|\boldsymbol{q}|)$, as depicted by the upper thick solid curve.

nonlinear term ($\lambda = 0$, EW) and to Equation 16 (WV), respectively. In the latter case, the suggestion that the WV equation models surface diffusion is confirmed by the fact that $-\nabla^4$ and q^4 are a Fourier transform pair. Thus, when $n = 4$, Equation 19 is merely the Fourier transform of Equation 16. There is no analytical expression for the Fourier transform of Equation 17 because of its nonlinear term. In the former case, the $\nabla^2 H(\boldsymbol{r})$ term in the KPZ equation is the inverse Fourier transform of $-|\boldsymbol{q}|^2 h(|\boldsymbol{q}|)$, and thus it represents the $n = 2$ smoothening mechanism of evaporation and recondensation, which should be more important at high growth temperatures. The nonlinear term that imposes rotational invariance on the KPZ equation models the effect of isotropic deposition on the growing surface, and it also does not have an analytic representation in reciprocal space. In principle, Equation 21 can be used with noninteger values of $n(\alpha)$ to provide analytic approximations for the spectral density functions for Equations 15 and 17, and any other scaling model as well, by using Equation 23 to obtain an effective value of n.

The complete spatial and temporal description of the surface morphology is contained in $g(|\boldsymbol{q}|, t)$, and in the case where there is only one dominant smoothening mechanism, $g(|\boldsymbol{q}|, t)$ is completely determined by only three parameters: n is derived from the identity of the smoothening mechanism, and c_n and Ω are system-dependent parameters. The mechanistic approach shows again that a complex physical system can be described by just a few numbers. Because these parameters are derived from the growth mechanism rather than the film geometry, one must compute $g(|\boldsymbol{q}|, t)$ as a function of $|\boldsymbol{q}|$ and t to obtain a surface rms and correlation length, as depicted in the series of log-log plots for $n = 2$, shown in Ref. 25a. By Parseval's theorem (25a), the radial integral of Equation 21 over $|\boldsymbol{q}|$ corresponds to the variance δ^2 of the surface height in real space, which allows the time dependence of the surface rms to be determined. As the low $|\boldsymbol{q}|$ plateau of $g(|\boldsymbol{q}|)$ moves up with increasing growth time, the knee in $g(|\boldsymbol{q}|)$, which represents the critical spatial frequency $|\boldsymbol{q}|_c$, moves to lower values of $|\boldsymbol{q}|$. The choice of the location of the knee in any one curve in Figure 14 is somewhat arbitrary, but once made and applied consistently to $g(|\boldsymbol{q}|, t)$ for all t, the time dependence of the correlation length $L_c = 1/q_c$ can also be determined.

A major advantage of the reciprocal-space representation of Equation 21 is that it can analytically model the effect of the smoothening processes of plastic flow ($n = 1$), which is important for smoothening of oxide surfaces (89), and bulk diffusion ($n = 3$) on surface morphology. However, the inverse Fourier transforms of $|\boldsymbol{q}|$ and $|\boldsymbol{q}|^3$ that represent these mechanisms in real space are extremely cumbersome and do not yield analytical solutions to their respective equations of motion. In addition, because all

the terms of the form represented by Equation 18 are linear, Equation 21 is easily generalized to the following form (22, 45):

$$g(|\boldsymbol{q}|, t) = \langle |h(\boldsymbol{q}, t)|^2 \rangle = \Omega \frac{1 - \exp(-2\Sigma c_n |\boldsymbol{q}|^n t)}{2\Sigma c_n |\boldsymbol{q}|^n}, \qquad 24.$$

which can be used to analytically represent the effect of two or more smoothening mechanisms acting simultaneously during surface growth. The primary problems with Equation 24 are that the nonlinear terms of Equations 15 and 17, if they are important, cannot be included in this analytical expression for the spectral density and that there is no corresponding analytical expression for the autocovariance function. $G(|\boldsymbol{r}|)$ must be obtained by numerically taking the inverse Fourier transform of $g(|\boldsymbol{q}|)$. The number of parameters required to totally specify $g(|\boldsymbol{q}|, t)$ is one (Ω) plus two times the number of active smoothening mechanisms (n, c_n) that contribute to the surface morphology, and the temporal dependence of L_c and δ have to be determined graphically or numerically from Equation 24 and its integral.

Nonstochastic Roughening by 3D Islanding

The $\sim|\boldsymbol{q}|^{-4}$ behavior of the spectral density for experimental systems (21, 45) at large q is described very well by Equation 24, but it cannot have a peak at $|\boldsymbol{q}| > 0$ for positive values of the constants c_n, as do the many experimental spectral densities described previously. Because stochastic roughening produces an essentially constant value for $g(|\boldsymbol{q}|)$ and smoothening causes a decrease in $g(|\boldsymbol{q}|)$ as $|\boldsymbol{q}|$ increases, the peak in $g(|\boldsymbol{q}|)$ must arise from another type of roughening mechanism. One example of roughening that has been considered is the phenomenon of shadowing (90), in which the initial peaks on the surface that result from stochastic processes shadow the surrounding areas of the surface after they reach a large enough size and then continue to grow more rapidly than their surroundings. Shadowing is considered to be most important for a totally isotropic flux of incident species, as opposed to the directed flux common in many surface growth techniques. Another type of roughening mechanism that has been discussed arises from surface diffusion on a very rough surface (91). For a small amount of surface roughness, the smoothening that arises from the $-c_n|\boldsymbol{q}|^4 h(|\boldsymbol{q}|, t)$ behavior of the rate of growth dominates, but as the surface becomes rougher, other terms in a more complete description of surface diffusion can appear with positive coefficients, and thereby give rise to roughening in addition to that arising from noise in the growth process. Even if the initial surface is completely smooth, the

Stranski-Krastanov and Volmer-Weber growth modes produce strong surface roughening for the case of heterodeposition because of the Grinfield instability (8). All of these cases can be considered to be different aspects of the more general category of island formation on growing surfaces, and they will introduce terms with a net positive sign in the growth (Equation 19).

Three-dimensional (3D) island growth processes are particularly simple to model mathematically by the scaling method of Herring (85). Surface roughening by island growth yields the following terms:

$$\frac{\partial h(|\boldsymbol{q}|, t)}{\partial t} \propto +c_5|\boldsymbol{q}|^1 + c_6|\boldsymbol{q}|^3, \qquad 25.$$

where the new coefficients are positive numbers and are preceded by plus signs to represent roughening. The exponent $n = 1$ in this case represents island growth dominated by deposition onto the surfaces of existing islands, and the exponent $n = 3$ represents the growth of islands caused by material that lands on the substrate and then diffuses to the islands (WM Tong & RS Williams, work in preparation). In the initial nucleation phase of growth, the second term in Equation 25 should dominate, and at later times when most of the surface is actually covered by islands, the first term should dominate. This adds a complication in that the coefficients c_5 and c_6 may be coverage and therefore time dependent, although in general we restrict ourselves to the case in which most of the surface is covered with islands and the c_5 term certainly dominates.

The approach that we have taken to model our data is to use a fitting function similar to Equation 24,

$$g(|\boldsymbol{q}|, t) \propto \Omega \frac{\exp(2\Sigma\chi_n|\boldsymbol{q}|^n t) - 1}{\Sigma\chi_n|\boldsymbol{q}|^n}, \qquad 26.$$

where the q-coefficients χ_n are simply fitting parameters. The q-coefficients in Equation 26 are allowed to take either positive or negative values, which will indicate if the corresponding q-dependence is a net roughening or smoothening process, respectively. Figure 13 illustrates how a growing surface with $\chi_3 > 0$ and $\chi_4 < 0$ can produce a spectral density function with a peak in $g(|\boldsymbol{q}|)$ at $|\boldsymbol{q}| > 0$ (89). Such a peak is caused by the existence and net dominance over a smoothening mechanism with the same q-dependence of a nonstochastic roughening mechanism, which is perhaps the most important insight to be gained from the mechanistic approach of modeling surface growth. Because the island growth mechanisms have the same q-dependence as smoothening by plastic flow and by volume diffus-

ion, the net values for two of the coefficients obtained by fitting Equation 26 to experimental data represent $\chi_1 = c_5 - c_1$ and $\chi_3 = c_6 - c_3$. Thus, if both island growth by deposition onto islands and plastic flow play a role in the evolution of a growing surface, one will dominate, and the net q-dependence will mask the fact that the other is present. This has the unfortunate effect of preventing the straightforward calculation of material-dependent properties from the parameters χ_n unless there is additional information about the smoothening or roughening processes.

Figure 14 shows the result of fitting the experimental $g(|\boldsymbol{q}|)$ data for the CuCl films grown on CaF_2 substrates from Figure 3 with Equation 26. As can be seen, this fitting function captures all of the important features of the experimental spectral density functions. The sign of the fitting parameters χ_n, which are shown in Table 2, indicates whether the corresponding smoothening or roughening mechanism is dominant. The fits for all four data sets are consistent in indicating that the primary roughening mechanisms are related to the $n = 1$ and $n = 3$ terms in Equation 26, that surface diffusion ($n = 4$) is the primary smoothening process, and that evaporation-recondensation ($n = 2$) may contribute significantly to the evolution of the surface morphology. However, in the present model, the

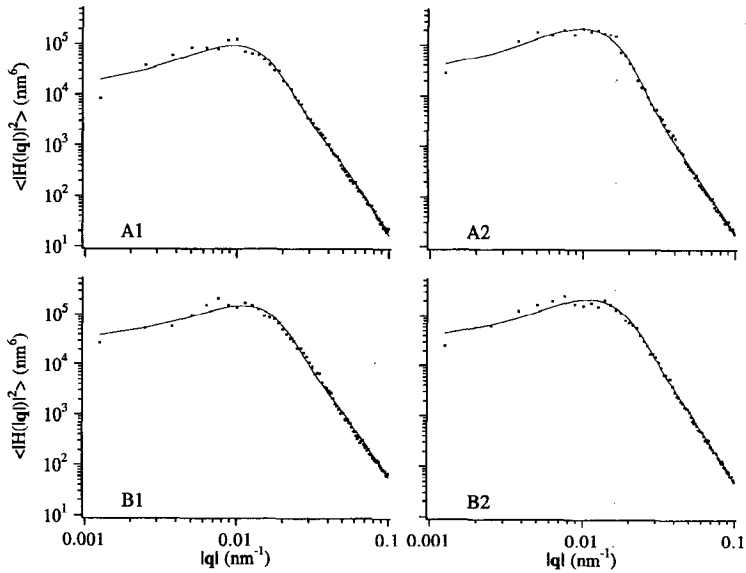

Figure 14 Fits of Equation 26 to the $g(|\boldsymbol{q}|)$ data for the CuCl films of Figure 3. The data are presented as log-log plots, which stress the high $|\boldsymbol{q}|$ behavior but suppress the peak that is very prominent on a linear scale, as are those of Figure 7*b*.

Table 2 Comparison of fits of Equation 26 to heteroepitaxial growth of CaF_2[a]

Sample	$\Omega(\times 10^3)$	t	$\chi_1(\times 10^2)$	$\chi_2(\times 10^4)$	$\chi_3(\times 10^5)$	$\chi_4(\times 10^6)$
A1	6.167	1	−3.968	2.989	−7.359	8.424
A2	6.385	2	−2.059	1.588	−4.521	6.769
B1	13.680	1	−2.965	1.923	−4.096	4.838
B2	7.321	2	−1.731	1.205	−2.944	3.408

[a] From Figure 14.

parameters χ all appear to be coverage or time dependent. Equation 26 may have to be modified to include the effects of nonlinear terms in the equation of motion for the growing surface such as those in Equations 13 and 15, or there may be additional smoothening or roughening mechanisms that have not yet been considered.

CONCLUSIONS

The complex morphologies that result from surface growth can be quantitatively described with just a very few parameters. The familiar phenomenological characterization scheme of specifying the surface rms (δ), the Gaussian-derived lateral correlation length (σ), and the spatial frequency (b) of the maximum spectral density provides a set of parameters that can be easily calculated from the autocovariance function and whose meanings are straightforward to visualize. The inadequacies of standard phenomenology are that this parameterization does not provide insight into either the origin of the surface features or the evolution of the structure, and the use of the minimum set of three parameters actually yields a rather poor approximation to the autocorrelation function and spectral density. Using an autoregressive approach with five parameters, one of them being the value of the spectral density at $|\boldsymbol{q}| = 0$, yields a much better description of the autocovariance and spectral density but without any physical meaning associated with the parameters. The reason why a fourth-order autoregression formula works well can be attributed to the fact that surface diffusion is important for the development of surface morphology, and it has a characteristic $|\boldsymbol{q}|^{-4}$ signature in the spectral density of the surface that is approximated by the fourth-order term in the autoregression.

The application of scaling analyses to surface growth was a major advance in the ability to predict the evolution of surface topology. In principle, the entire spatial and temporal dependence of the evolution of a surface is contained in only five numbers: the universal static and dynamic

scaling exponents (α, β), the material-dependent surface rms height, and the critical length for scaling [$\delta(\tau), L_c(\tau)$] measured at some particular time (τ). With this information, the rms and the critical or correlation length can be predicted for all times t from the scaling relations of Equations 12 and 13, and at any given time, the autocovariance function and the spectral density can be calculated by Equations 10 and 11. This approach demonstrates that there is a great underlying simplicity to surface growth. However, the scaling exponents do not appear to be universal and more importantly, the scaling relations of Equations 10 and 11 cannot account for the fact that the spectral density for many real systems has a peak at a nonzero spatial frequency.

The continuum models for surface growth provide insight into some of the specific mechanisms behind the scaling exponents. In particular, scaling analyses demonstrate that surface diffusion by itself cannot produce a flat surface in the presence of stochastic roughening. The length scale over which surface diffusion acts is too small to be effective beyond a locally flat but tilted facet. Rather, surface diffusion with random noise yields a self-similar morphology for which both the surface rms height and the correlation length increase with growth time as $t^{1/4}$. The only continuum equation that can yield the types of flat surfaces observed for MBE growth is the EW equation (Equation 15 with $\lambda = 0$). This equation corresponds to stochastic roughening with smoothening by evaporation and recondensation. Because the vapor pressure of a convex curved surface is higher than that of a planar surface (92), at the high temperatures required for high-quality epitaxial growth, islands will sublime whereas flat areas will be favored condensation regions. The length scale for smoothening by evaporation and recondensation is large enough to create a globally flat surface if stochastic noise is the only significant roughening mechanism in the system.

The mechanistic approach to modeling the spatial and temporal dependence of growing surfaces has both advantages and disadvantages compared with scaling analysis. The spectral density of a growing surface in reciprocal space and time $g(|\boldsymbol{q}|, t)$ is defined with a fairly simple analytical expression in Equation 26 when considering only the linear mechanisms of smoothening and roughening. This expression can be adapted to include the simultaneous action of all four of the major linear smoothening mechanisms, including plastic flow and bulk diffusion, which cannot be handled analytically in a real-space equation of motion. It can also readily include the roughening terms that arise from the nucleation and growth of islands on a surface. This nonstochastic roughening is responsible for the peaks that appear in the spectral density functions of grown surfaces at $|\boldsymbol{q}| > 0$.

Equation 26 also provides insight into why experimental values of the static scaling exponent α often agree closely with the theoretical predictions of the continuum theories of Equations 16 and 17, whereas the experimental dynamic scaling exponents β are often much greater than the theories allow. The exponent α is related through Equation 23 to the large $|\boldsymbol{q}|$ slope of $g(|\boldsymbol{q}|)$ vs $|\boldsymbol{q}|$ on a log-log plot, and because surface diffusion with $n = 4$ is a major factor in the formation of surface morphology, the effective value of $\alpha \approx 1$ will be determined from plots of $\log(\xi)$ vs $\log(L)$ for these cases. However, the value of $\delta(t)$ is determined by integrating $g(\boldsymbol{q}, t)$ over $\boldsymbol{q}$, and the presence of a nonstochastic roughening term in Equation 26 will significantly increase the temporal derivative of $\delta(t)$. The effective value of β determined from log-log plots of δ vs growth time will thus be larger than predicted by scaling analyses because they do not include nonstochastic roughening.

In the general case, nine parameters are required to completely define $g(\boldsymbol{q}, t)$: the value of Ω and the four pairs of numbers represented by (n, χ_n) in Equation 26. Although in principle the values of χ_n are related to basic physical constants of the system, such as diffusion constants and surface energies, the values of the parameters obtained from fitting experimental spectral-density functions can contain offsetting contributions from both smoothening and roughening mechanisms. The parameters χ_n can be used to obtain a very good approximation to the experimental $g(|\boldsymbol{q}|)$, but they are not related in an analytic fashion to structural parameters such as the surface rms or correlation length. These must be obtained numerically or graphically from $g(|\boldsymbol{q}|)$. In fact, each smoothening or nonstochastic roughening mechanism will have its own characteristic correlation length that can be determined from a plot of Equation 21 for a single pair of q-coefficient and related q-exponent. Even though the $g(|\boldsymbol{q}|)$ from Equation 26 is a major improvement over previous approximations, it does not correctly predict the time dependence of the spectral-density function for growing CuCl films, as shown in Table 2. At present, it is unclear whether the changes required to make Equation 26 a truly predictive tool for understanding the development of the topology of growing surfaces are minor or if a different approach must be developed. The recent theoretical work of Amar & Family (91) is notable for predicting the shape of the $G(|\boldsymbol{r}|)$ curve for their model of surface diffusion. In the future, both experimental and theoretical investigations should concentrate on obtaining the functional form of the autocovariance $G(|\boldsymbol{r}|, t)$ and/or the spectral density $g(|\boldsymbol{q}|, t)$ over the largest possible range of length or spatial frequency and time, because these are the most complete and sensitive characteristics of rough growing surfaces.

ACKNOWLEDGMENTS

We gratefully acknowledge the assistance of and helpful conversations with MS Anderson, R Bruinsma, E Chason, TM Mayer, RPU Karunisari, EA Eklund, T Ngo, EJ Snyder, and especially J Rudnick. The research performed by the authors in this field has been supported by the National Science Foundation and the Office of Naval Research.

Literature Cited

1. Bauer E. 1958. *Z. Kristallogr.* 110: 372–431
2. Frank FC, van der Merwe JH. 1949. *Proc. R. Soc. Lond. Ser. A* 198: 205–16
3. Volmer M, Weber A. 1926. *Z. Phys. Chem.* 119: 277–301
4. Stranski IN, Kr'stanov L. 1938. *Sitzungsber. Akad. Wiss. Wien* 146: 797–810
5. Bauer E, van der Merwe JH. 1986. *Phys. Rev. B* 33: 3657–71
6. Kern R, LeLay G, Metois JJ. 1980. In *Current Topics in Materials Science*, ed. E Kaldis, pp. 133–419. Amsterdam: North-Holland
7. van der Merwe JH. 1991. *Crit. Rev. Solid State Mater. Sci.* 17: 187–209
8. Grinfeld MA. 1993. *J. Intell. Mater. Syst. Struct.* 4: 76–81
9. Bauer EG, Dodson BW, Ehrlich DJ, Feldman LC, Flynn CP, et al. 1990. *J. Mater. Res.* 5: 852–94
10. Argile C, Rhead GE. 1989. *Surf. Sci. Rep.* 10: 277–356
11. Rhead GE, Barthes MG, Argile C. 1981. *Thin Solid Films* 82: 201–11
12. Burton WK, Cabrera N, Frank FC. 1951. *Philos. Trans. R. Soc. London Ser. A* 243: 299–358
13. Venables JA, Spiller GDT, Hanbucken M. 1984. *Rep. Prog. Phys.* 47: 399–459
14. Venables JA. 1986. *J. Vac. Sci. Technol. B* 4: 870–73
15. Kajikawa Y, Hata M, Isu T, Katayama Y. 1992. *Surf. Sci.* 265: 241–51
16. Wheeler AA, Ratsch C, Morales A, Cox HM, Zangwill A. 1922. *Phys. Rev. B* 46: 2428–34
17. Ghez R, Cohen HG, Keller JB. 1990. *Appl. Phys. Lett.* 56: 1977–79
18. Nieminen JA, Kaski K. 1987. *Surf. Sci. Lett.* 185: 489–96
19. Nieminen JA, Kaski K. 1989. *Phys. Rev. A* 40: 2088–95
20. Neddermeyer H. 1990. *Crit. Rev. Solid State Mater. Sci.* 16: 309–35
21. Tong WM, Snyder EJ, Williams RS, Yanase A, Segawa Y, Anderson MS. 1992. *Surf. Sci. Lett.* 277: 63–70
22. Bales GS, Bruinsma R, Eklund EA, Karunasiri RPU, Rudnick J, Zangwill A. 1990. *Science* 249: 264–68
23. Golubovic L, Bruinsma R. 1991. *Phys. Rev. Lett.* 66: 321–24
24. Eklund EA, Snyder EJ, Williams RS. 1993. *Surf. Sci.* 285: 157–80
25. Rasigni G, Varnier F, Rasigni M, Palmari JP, Llabaria A. 1983. *Phys. Rev. B* 27: 819–30
25a. Stearns DG. 1993. *Appl. Phys. Lett.* 62: 1745–47
26. Rasigni M, Rasigni G, Varnier F, Dussert C, Palmari J, et al. 1988. *SPIE Surf. Meas. Charact.* 1009: 68–76
27. Elson JM, Bennett HE, Bennett JM. 1979. In *Applied Optics and Optical Engineering*, ed. RR Shannon, JC Wyant, 7: 191–244
28. Maradudin AA. 1982. In *Surface Polaritons, Electromagnetic Waves at Surfaces and Interfaces*, ed. VM Agranovitch, DL Mills, p. 405. Amsterdam: North-Holland
29. Kretschmann E. 1972. *Opt. Commun.* 5: 331–36
30. Kroger E, Kretschmann E. 1970. *Z. Phys.* 237: 1–15
31. Kretschmann E. 1974. *Opt. Commun.* 10: 353–56
32. Varnier F, Dussert C, Rasigni G, Rasigni M, Llabaria A. 1988. *J. Vac. Sci. Technol. A* 6: 1627–30
33. Rasigni G, Lafraxo M, Buat V, Rasigni M, Abdellani F, Llabaria A. 1993. *J. Opt. Soc. Am. A* 10: 1257–62

34. Mandlebrot B. 1983. In *The Fractal Geometry of Nature*, p. 468. New York: Freeman
35. Mitchell MW, Bonnell DA. 1990. *J. Mater. Res.* 5: 2244–54
36. Varnier F, Llabaria A, Rasigni G. 1990. *J. Vac. Sci. Technol. A* 8: 1554–59
37. Krug J, Spohn H. 1992. In *Solids Far From Equilibrium*, ed. C Godreche, pp. 479–582. New York: Cambridge Univ. Press
38. Rudnick J, Bruinsma R. 1994. In *Low Energy Ion-Surface Interactions*, ed. JW Rabalais, pp. 535–59. New York: Wiley
39. Williams RS, Bruinsma R, Rudnick J. 1992. *Proc. Mater. Res. Soc. Symp.* 231: 269–86
40. Steyer A, Guenoun P, Beysens D, Knobler CM. 1991. *Phys. Rev. A* 44: 8271–77
41. Fritter D, Knobler CM, Beysens DA. 1991. *Phys. Rev. A* 43: 2858–69
42. Beysens D, Knobler CM. 1986. *Phys. Rev. Lett.* 57: 1433–36
43. Viovy JL, Beysens D, Knobler CM. 1988. *Phys. Rev. A* 37: 4965–70
44. Beysens D, Knobler CM, Schaffar H. 1990. *Phys. Rev. B* 41: 9814–18
45. Eklund EA, Bruinsma R, Rudnick J, Williams RS. 1991. *Phys. Rev. Lett.* 67: 1759–62
46. Bradley RM, Harper JME. 1988. *J. Vac. Sci. Technol. A* 6: 2390–95
47. Carter G, Nobes MJ, Whitton JL. 1985. *Appl. Phys. A* 38: 77–95
48. Chason E, Mayer TM. 1993. *Appl. Phys. Lett.* 62: 363–65
49. Krim J, Heyvaert I, Haesendonck CV, Bruynsraede Y. 1993. *Phys. Rev. Lett.* 70: 57–60
50. Vicsek T. 1992. In *Fractal Growth Phenomena*, pp. 200–6. Hong Kong: World
51. Zangwill A. 1993. *Mater. Res. Soc. Symp. Prod.* 280: 121–30
52. Family F, Vicsek T. 1985. *J. Phys. A* 18: 75–79
53. You H, Chiarello RP, Kim HK, Vandervoort KG. 1993. *Phys. Rev. Lett.* 70: 2900–3
54. Berry MV. 1973. *Philos. Trans. R. Soc. London Ser. A* 273: 611–17
55. Family F. 1990. *Physics A* 168: 561–80
56. Zhang Z, Detch J, Metiu H. 1993. *Phys. Rev. B* 48: 4972–75
57. Forrest BM, Tang L-H. 1990. *Phys. Rev. Lett.* 64: 1405–8
58. Kardar M, Parisi G, Zhang Y-C. 1986. *Phys. Rev. Lett.* 56: 889–92
59. Edwards SF, Wilkinson DR. 1982. *Proc. R. Soc. London Ser. A* 381: 17–31
60. Sudijono J, Johnson MD, Elowitz MB, Snyder CW, Orr BG. 1993. *Surf. Sci.* 280: 247–50
61. Das Sarma S, Ghaisas SV. 1992. *Phys. Rev. Lett.* 69: 3762–65
62. Das Sarma S, Lai Z-W, Tamborenea P. 1992. *Surf. Sci. Lett.* 268: 311–18
63. Hwa T, Kardar M, Paczuski M. 1992. *Phys. Rev. Lett.* 66: 441–44
64. Kessler DA, Levine H, Sander LM. 1992. *Phys. Rev. Lett.* 69: 100–3
65. Krug J, Plischke M, Siegert M. 1993. *Phys. Rev. Lett.* 70: 3271–74
66. Lai Z-W, Das Sarma S. 1991. *Phys. Rev. Lett.* 66: 2348–51
67. Maritan A, Toigo F, Koplik J, Banavar JR. 1992. *Phys. Rev. Lett.* 69: 3193–95
68. Nattermann T, Tang L-H. 1992. *Phys. Rev. A* 45: 7156–61
69. Tamborenea PI, Lai Z-W, Das Sarma S. 1992. *Surf. Sci.* 267: 1–4
70. Tang L-H, Natterman T. 1991. *Phys. Rev. Lett.* 66: 2899–902
71. Villain J. 1991. *J. Phys. I* 1: 19–42
72. Wolf DE, Villain J. 1990. *Europhys. Lett.* 13: 389–94
73. Yan H. 1990. *Phys. Rev. Lett.* 64: 926–29
74. Yan H. 1992. *Phys. Rev. Lett.* 68: 3048–51
75. Salvarezza RC, Vazquez L, Herrasti P, Ocon P, Vara JM, Arvia AJ. 1992. *Europhys. Lett.* 20: 727–32
76. Ngo T, Snyder EJ, Tong WM, Williams RS, Anderson MS. 1994. *Surf. Sci.* In press
77. Ngo T, Brandt L, Williams RS, Kaesz HD. 1993. *Surf. Sci.* 291: 411–18
78. Woronick SC, Ng W, Krol A, Kao YH, Arnold E. 1991. *J. Appl. Phys.* 69: 1631–42
79. Chason E, Warwick DT. 1991. *Mater. Res. Soc. Symp. Proc.* 208: 351–56
80. Chason E, Mayer TM, Payne A, Wu D. 1992. *Appl. Phys. Lett.* 60: 2353–55
81. Chason E, Mayer TM, McIlroy D, Matzke CM. 1993. *Nucl. Instrum. Methods Phys. Res. B* 80/81: 742–46
82. Chiarello R, Panella V, Krim J, Thompson C. 1991. *Phys. Rev. Lett.* 67: 3408–11
83. He Y-L, Yang H-N, Lu T-M, Wang G-C. 1992. *Phys. Rev. Lett.* 69: 3770–73
84. Zuo J-K, Wendelken JF. 1993. *Phys. Rev. Lett.* 79: 1662–65
84a. Tong WM, Williams RS, Yanase A, Segawa Y, Anderson MS. *Phys. Rev. Lett.* 72: 3374–77
85. Herring C. 1950. *J. Appl. Phys.* 21: 301–3
86. Mullins WW. 1959. *J. Appl. Phys.* 30: 77–83
87. Vvedensky DD, Zangwill A, Luse CN,

Wilby MR. 1993. *Phys. Rev. E* 48: 852–62
88. Bruinsma R, Karunasiri RPU, Rudnick J. 1990. In *Kinetics of Ordering and Growth at Surfaces*, ed. MG Lagally, pp. 395–402. New York: Plenum
89. Mayer TM, Chason E, Howard AJ. 1994. *J. Appl. Phys.* 76: 1–9
90. Karunasiri RPU, Bruinsma R, Rudnick J. 1989. *Phys. Rev. Lett.* 62: 788–91
91. Amar JG, Family F. 1993. *Phys. Rev. E* 47: 1595–603
92. Thomson W. 1871. *Philos. Mag.* 42: 448–56